

ORIGINAL ARTICLE

Tailoring of the trap distribution and crystal field in Cr³⁺-doped non-gallate phosphors with near-infrared long-persistence phosphorescence

Yang Li^{1,2,3}, Yiyang Li⁴, Ruchun Chen¹, Kaniyarakkal Sharafudeen⁵, Shifeng Zhou^{1,2}, Mindaugas Gecevicius⁶, Haihui Wang³, Guoping Dong^{1,2}, Yiling Wu^{1,2}, Xixi Qin^{1,2} and Jianrong Qiu^{1,2}

We present a series of efficient near-infrared (NIR) Cr³⁺-doped non-gallate long-persistence phosphors (Zn₂SnO₄: Cr and Zn_(2-x)Al_{2x}Sn_(1-x)O₄: Cr) and highlight their special optical characteristics of broad emission band (650–1200 nm, peaking at 800 nm) and long afterglow duration (> 35 h). In the context of materials selection, these systems successfully avoid the existing ubiquitous reliance on gallates as hosts in Cr³⁺-doped phosphorescent phosphors. Zn₂SnO₄ is employed as a host to take advantage of its characteristic inverse spinel crystal structure, easy substitution into Zn²⁺ and Sn⁴⁺ sites by Cr³⁺ in distorted octahedral coordination and non-equivalent substitution. In this work, Al dopant was introduced both to precisely tailor the local crystal field around the activator center, Cr³⁺, and to redeploy trap distribution in the system. Indeed, such redeployment permits band gap adjustment and the dynamic variation of the annihilation and the formation of defects. The results demonstrate that the method employed here can be an effective way to fabricate multi-wavelength, low-cost, NIR phosphorescent phosphors with many potential multifunctional bio-imaging applications.

NPG Asia Materials (2015) 7, e180; doi:10.1038/am.2015.38; published online 22 May 2015

INTRODUCTION

Long-phosphorescence phosphors (LPPs), also called long-lasting, long-persistence or long-duration phosphors, have been widely applied in safety signage, dial displays, security ink, night-vision surveillance and *in vivo* bio-imaging because of their unique energy storage ability.^{1,2} In particular, they possess many advantages over other biomarkers for potential use in *in vivo* imaging applications. To date, various advanced fluorescent tags such as fluorescent dyes, metal nanoparticles, semiconductor quantum dots and upconversion nanoparticles have been proposed and successfully applied to *in vivo* bio-imaging.^{3–5} Biomarkers with persistent phosphorescence in the near-infrared (NIR) window (650–1350 nm) have already proven their superiority in biological tissue over other labels because their persistence time is sufficiently long to permit time-gated imaging. As a result, they avoid the challenging requirement of high-intensity illumination during signal collection, which often leads to increased signal-to-noise ratio and photon-induced deterioration of analytes.⁶ Such biomarkers are expected to enable advanced optical imaging with high-resolution and minimal excitation disturbance to experimentally assess structural and functional processes in cells, tissues and other complexes in *in vivo* systems.⁷

Over the past few years, substantial strides have been made in the research and development of LPPs for NIR wavelengths,^{8–20} with the main focus of the research being Mn²⁺, Mn⁴⁺ and Cr³⁺-activated NIR LPPs. In 2007, Chermont *et al.* proposed a novel bio-imaging method using red-to-NIR persistent nanoparticles, Ca_{0.2}Zn_{0.9}Mg_{0.9}Si₂O₆: Eu²⁺, Dy³⁺, Mn²⁺, and opened a new application area for NIR LPPs.⁶ In 2012, Pan *et al.* broke new ground in the field by using gallates as the system, thereby achieving a super-long NIR afterglow emission time of 360 h in the Zn₃Ga₂Ge₂O₁₀: Cr³⁺ phosphor and firmly establishing gallates as the preferred material system for the fabrication of Cr³⁺-activated NIR LPPs. In addition to ZnGa₂O₄: Cr³⁺, La₃Ga₅GeO₁₄: Cr³⁺, LiGa₅O₈: Cr³⁺, Ga₂O₃: Cr³⁺ and Gd₃Ga₅O₁₂: Cr³⁺ phosphors, the afterglow properties of many other Cr³⁺-activated gallate phosphors, such as Zn₃Ga₂SnO₈: Cr³⁺, MgGa₂O₄: Cr³⁺, Ca₃Ga₂Ge₃O₁₂: Cr³⁺ and SrGa₁₂O₁₉: Cr³⁺, were investigated because of the excellent ability of Cr³⁺ ions to substitute for Ga³⁺ ions in distorted octahedral coordination.^{9–20} The predominance of Cr³⁺-activated gallates might suggest that only gallates can be used as the hosts in Cr³⁺-doped NIR LPPs. Such a dependence would result in the trapping and de-trapping processes being closely associated with the crystalline structure or energy band structure, of gallates because a variety of defects in gallate

¹State Key Laboratory of Luminescent Materials and Devices, School of Materials Science and Technology, South China University of Technology, Guangzhou, China; ²Guangdong Provincial Key Laboratory of Fiber Laser Materials and Applied Techniques, Guangzhou, China; ³School of Chemistry and Chemical Engineering, South China University of Technology, Guangzhou, China; ⁴Henry Samueli School of Engineering, University of California, Irvine, CA, USA; ⁵Escola de Engenharia de Sao Carlos, Universidade de Sao Paulo, Sao Carlos, Brazil and ⁶Optoelectronics Research Centre, University of Southampton, Southampton, UK

Correspondence: Professor J Qiu, State Key Laboratory of Luminescent Materials and Devices, School of Materials Science and Technology, South China University of Technology, Guangzhou 510640, China.

E-mail: qjr@scut.edu.cn

Received 16 August 2014; revised 18 March 2015; accepted 19 March 2015

materials, including antisite defects and Ga vacancies, have been proposed as an electron (or hole) reservoir to improve the afterglow properties.^{7–10} However, it is challenging to identify the nature of defects and it is difficult to predict the actual effectiveness and impact of intrinsic and substituted defects in gallates because comparison with Cr³⁺-doped non-gallate phosphors is missing. To date, there have been no convincing proposals of an effective alternative system that might replace gallates as the preferred host for achieving super-long NIR afterglow emissions. Thus, the investigation carried out here on Cr³⁺-activated non-gallate phosphors is expected to be beneficial in identifying alternative hosts and developing a new understanding of the afterglow mechanisms of Cr³⁺-doped LPPs. In addition, considering the high cost of gallates, it would be further advantageous if the new Cr³⁺-activated non-gallates were also earth-abundant and inexpensive.

It is also worth noting that in NIR LPP applications, working bands and persistence times are the two key aspects that need to be considered when optimizing the bio-imaging conditions. An important issue is the dissimilarities in NIR optical windows across different tissues types in the living body.²¹ Ideally, a brilliant NIR phosphorescent phosphor would offer superior afterglow emission that could accurately cover the biologically transparent window. Although effort has been directed toward realizing this goal, it is not a trivial undertaking to explore the appropriate NIR emission centers and, furthermore, to flexibly tune the emission band to the desired band by adjusting the crystal field surrounding the dopant. However, it is worth investigating the simple but effective approach of tuning the operation band by slightly varying the LPP composition because of the potential widespread applicability of this concept to develop novel structural and functional materials with persistent phosphorescence. Unfortunately, few reports have addressed novel activation centers or LPPs with tunable NIR emission.^{1,2,17,18,22} In regard to persistence time, it is well known that the trap distributions, including trap types, concentrations and depths in different materials are complicated and confusing because of the randomness and ephemeral nature of defects;²³ consequently, it is also challenging to successfully control the persistence time (which is dictated by trap distribution), let alone the synchronous control of emission wavelength and persistence time in the same phosphor by using the simple strategy discussed above.

To address these issues, we have developed earth-abundant NIR-phosphorescent Cr³⁺-doped non-gallate materials, (Zn₂SnO₄: Cr and Zn_(2-x)Al_{2x}Sn_(1-x)O₄: Cr). Here we list the attributes of this work in brief: (1) Low-cost Zn₂SnO₄: Cr phosphors with NIR long-persistence phosphorescence are enabled by a characteristic inverse spinel crystal structure, easy substitution in Zn²⁺ or Sn⁴⁺ sites by Cr³⁺ in distorted octahedral sites as a result of their identical ionic radius, and the

various types of defects that result from non-equivalent substitution. (2) We obtain a broad emission band from 650–1200 nm that peaks at 800 nm and a persistence time of > 35 h in Zn₂SnO₄: Cr phosphors. (3) Precise tailoring of the local crystal field around the activator center, Cr³⁺, and effective deployment of trap distributions are realized by adding only one extra element, aluminum, (that is, by changing the composition of the Zn_(2-x)Al_{2x}Sn_(1-x)O₄ solid solution), to obtain a tunable emission wavelength and persistence time. (4) The infrared phosphorescence peak positions can be precisely tuned from 800 to 720 nm by rearranging the ligands surrounding Cr³⁺ and by altering the electronic configuration of the central active element through the addition of Al. (5) It is revealed that the deepening of trap site levels caused by the increasing energy gap between the conduction band (CB) level and the trap site level, along with the variation in trap concentration and type, which is determined by the dynamic variation of defect annihilation and creation, are both related to the phosphorescence duration of Zn_(2-x)Al_{2x}Sn_(1-x)O₄ phosphors, as demonstrated by the thermoluminescence (TL) spectra and electron spin resonance (ESR) measurements.

MATERIALS AND METHODS

Materials

Pure Al₂O₃ (4 N), SiO₂, GeO₂, SnO₂, ZnO and Cr₂O₃ were selected as the raw materials.

Preparation of Zn_{2-x}Al_{2x}Sn_{1-x}O₄ phosphors

Phosphors with molar compositions of Zn_{2-x}Al_{2x}Sn_{1-x}O₄: 0.2% Cr³⁺ (Table 1) were prepared by the solid-state reaction method. The reaction included a two-step thermal treatment (that is, initial calcination at 900 °C for 12 h, secondary calcination at 1450 °C for 12 h).

Preparation of Zn₂SiO₄ and Zn₂GeO₄ phosphors

Phosphors with molar compositions of Zn₂SiO₄: 0.2% Cr³⁺ and Zn₂GeO₄: 0.2% Cr³⁺ were prepared by the solid-state reaction method. The reaction included a two-step thermal treatment (that is, initial calcination at 900 and 700 °C for 12 h, secondary calcination at 1350 and 1150 °C for 12 h).

Characterization

The prepared materials were analyzed by X-ray diffraction (Cu/Kα), which confirmed the presence of Zn₂SiO₄, Zn₂GeO₄ or Zn₂SnO₄ (Supplementary Figure S2) as the sole crystalline phase. To investigate the presence of paramagnetic defects, ESR spectra were recorded with an X-band spectrometer (Germany, AXS, GmbH, Bruker A300) from the samples before and after irradiation by a xenon lamp. Room-temperature photoluminescence (PL), PL excitation (PLE) spectra, afterglow spectra and decay curves were measured with a high-resolution spectrofluorometer (UK, Edinburgh Instruments, FLS920) equipped with a 500 W Xenon lamp as an excitation source, with a Hamamatsu R928P visible photomultiplier (250–850 nm) and a liquid nitrogen-cooled Hamamatsu R5509-72 NIR photomultiplier as the detectors. TL glow curves and TL excitation (TLE) spectra were measured with a FJ-427 A TL meter (Beijing, China) to characterize the defect properties. Unless otherwise mentioned, the samples were pre-annealed at 600 K before testing and some measurements were taken after pre-irradiating the samples for 10 min by using a xenon lamp. X-ray photoelectron spectra (XPS, Kratos Axis Ultra DLD, Shimadzu, Kyoto, Japan) were measured by the physical electronics 5600 multi-technique system. Achromatic 150 W Al Kα X-rays were chosen as the excitation source. The resolution was 0.05 eV. Diffuse reflection spectra were obtained using a UV-Vis-NIR spectrometer (Agilent, Palo Alto, CA, USA, Cary 5000). Custom-built equipment was used to record the absolute afterglow intensity (Supplementary Figure S3). NIR imaging was performed with a modified imaging system including a Germany Pco Dicom Pro camera as the signal collector. Analysis and post processing of images were conducted by using a custom-written software.

Table 1 Chemical compositions of Zn₂MO₄: 0.2% Cr³⁺ (M = Si, Ge and Sn) and Zn_{2-x}Al_{2x}Sn_{1-x}O₄: 0.2% Cr³⁺ (x = 0.001, 0.005, 0.01, 0.05, 0.1, 0.2, 0.4, 0.8) phosphors

No	Composition	No	Composition
ZS1	Zn ₂ SiO ₄ : 0.2% Cr ³⁺	ZS8	Zn _{1.9} Sn _{0.9} Al _{0.2} O ₄ : 0.2% Cr ³⁺
ZG2	Zn ₂ GeO ₄ : 0.2% Cr ³⁺	ZS9	Zn _{1.8} Sn _{0.8} Al _{0.4} O ₄ : 0.2% Cr ³⁺
ZS3	Zn ₂ SnO ₄ : 0.2% Cr ³⁺	ZS10	Zn _{1.6} Sn _{0.6} Al _{0.8} O ₄ : 0.2% Cr ³⁺
ZS4	Zn _{1.999} Sn _{0.999} Al _{0.002} O ₄ : 0.2% Cr ³⁺	ZS11	Zn _{1.2} Sn _{0.2} Al _{1.6} O ₄ : 0.2% Cr ³⁺
ZS5	Zn _{1.995} Sn _{0.995} Al _{0.01} O ₄ : 0.2% Cr ³⁺	ZS12	Zn ₂ SnO ₄
ZS6	Zn _{1.99} Sn _{0.99} Al _{0.02} O ₄ : 0.2% Cr ³⁺	ZS13	Zn _{1.8} Sn _{0.8} Al _{0.4} O ₄
ZS7	Zn _{1.95} Sn _{0.95} Al _{0.1} O ₄ : 0.2% Cr ³⁺		

Abbreviation: No, number.

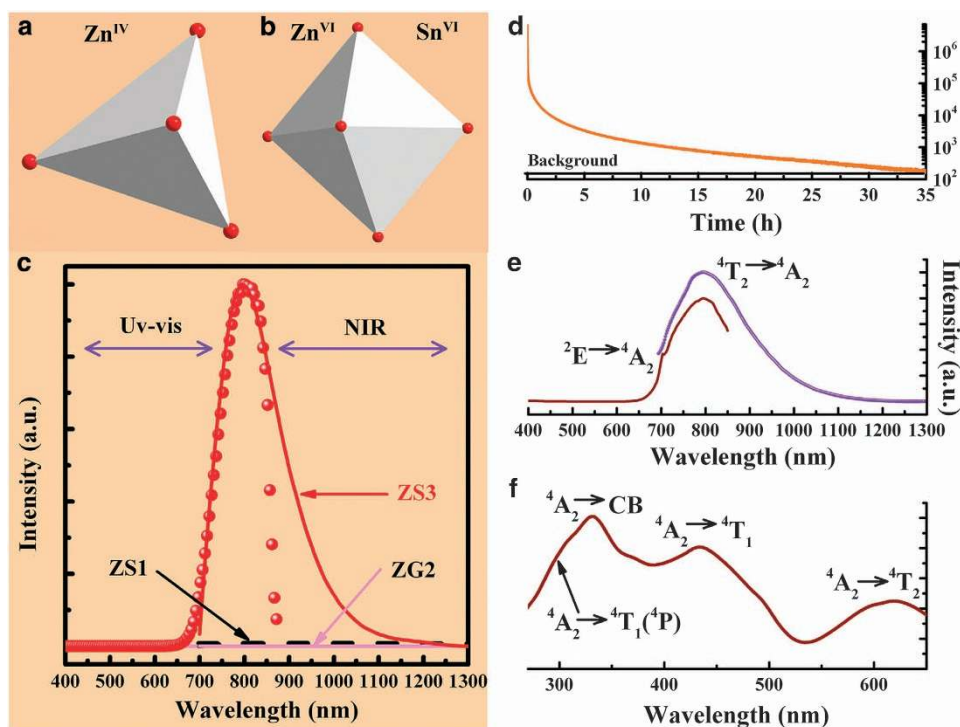


Figure 1 Long-persistence phosphorescence of Zn_2SnO_4 : Cr phosphor. (a, b) Octahedral and tetrahedral geometry of Zn_2SnO_4 ; (c) normalized Vis-near-infrared (NIR) long-persistence phosphorescence spectra of ZS1 (black dotted line), ZG2 (pink line) and ZS3 (red dot and curve) phosphors. The red dot line and curve are measured by visible light and NIR detection, respectively. The measurements were taken 1 min after irradiation ceased; (d) afterglow decay curve monitored at 800 nm emission; (e, f) normalized PL spectra in the visible and NIR regions excited at 330 nm and PL excitation spectra monitored at 800 nm emission of ZS3 sample. Before the measurements, the phosphors were pre-annealed at 600 K.

RESULTS AND DISCUSSION

Design strategy of Zn_2SnO_4

When designing LPPs with desirable photoemission wavelengths for practical applications, prioritized consideration must be given to identifying a suitable emitter because the emitters are centers that are capable of emitting radiation after being excited; they also determine emission wavelength. The easy and effective method that we propose for extending emission wavelength is to tailor the crystal field surrounding the emission center. It can be observed that among the numerous activation centers, rare earth ions exhibiting extremely sharp emission bands cannot meet this demand because $4f$ orbitals of lanthanide metal ions are effectively shielded from the influence of external forces by overlapping $5s^2$ and $5p^6$ orbitals.²⁴ Consequently, it is very difficult—even by varying the host material—to tune the emission bands by using rare earth ions as activators. In contrast to such rare earth ions, the hallmark of transition metal ions is that the electrons in their outermost d orbital strongly interact with their ligands and that the electronic configuration of the activation ions is affected strongly by the arrangement of surrounding ligands.^{23,25} By increasing the quantity of surrounding ligands and by shortening the distances between TM ions and ligands, the crystal field strength of TM ions can be increased. As a result, energy level splitting increases, which results in a shift in emission wavelength.²⁶ In this work, the Cr^{3+} ion was selected as the emission center after carefully weighing its potential for wavelength tunability by tailoring the local crystal field around Cr^{3+} sites. The dominant emission peak of a Cr^{3+} center in different hosts is expected to produce a shift arising from the altered crystal field strength.

Once an activation ion is selected, attention must be paid to a proper host material that is capable of creating appropriate defects.

It is generally accepted that either efficient intrinsic defects or intentionally introduced defects—or both—favorably increase the afterglow duration. With the rational selection of a defect-abundant host, the persistence time can be improved significantly. For example, Cr^{3+} -activated ZnGa_2O_4 phosphors with a cubic normal spinel crystal structure exhibit the remarkable feature of long-persistence phosphorescence, which is enabled by the $\sim 3\%$ fraction of antisite defects in the host materials.^{9,11} It should be noted that as an important ternary oxide semiconductor with high electron mobility and high electrical conductivity, Zn_2SnO_4 is widely used in gas sensors and as the photocatalyst and photoanode for dye-sensitized solar cells because of intrinsic defects that include oxygen vacancies and interstitial Zn, among others.^{27–29} Zinc stannate (Zn_2SnO_4) has a typical inverse spinel crystal structure with a band gap of ~ 3.6 – 3.7 eV (Supplementary Figure S1a).²⁷ Compared with normal spinel, the inverse spinel structure features an alternative cation arrangement. In Zn_2SnO_4 , all of the $[\text{Sn}^{\text{VI}}]$ cations and half of the $[\text{Zn}^{\text{VI}}]$ cations occupy octahedral sites, whereas the other half of the $[\text{Zn}^{\text{IV}}]$ cations occupy tetrahedral sites (Figure 1a and b)²⁹ This configuration thus features a path of easy doping ion precipitation into the octahedral $[\text{Sn}^{\text{VI}}]$ or $[\text{Zn}^{\text{VI}}]$ under the condition of matching geometrical lattice and atomic radius, which occurs with aluminum, chromium, gallium and others. On the basis on this arrangement, in addition to the intrinsic Zn vacancies and Zn interstitials, some antisite defects (such as $[\text{Sn}^{\text{VI}}]$ and $[\text{Zn}^{\text{VI}}]$ cations, which can freely exchange places in octahedral sites) and non-equivalent substitutional defects (Sn_{Cr} or Zn_{Cr}) are expected to be formed. These defects are expected to play an important role in the afterglow emission.

Long-persistence phosphorescence of Zn₂SnO₄: Cr phosphor

As anticipated, long-persistence phosphorescence from 650–1200 nm with the main emission peak at 800 nm was detected in Zn₂SnO₄: Cr³⁺ phosphor (sample ZS3) after excitation by a xenon lamp for 10 min (Figure 1c), which confirmed that the existent defects are energy reservoirs that can store electrons (or holes). This phosphor demonstrated a long afterglow duration of >35 h in the 800-nm emission band (Figure 1d). To determine whether Cr³⁺ participates in the phosphorescence emission process, it is necessary to analyze the steady-state PL and PL excitation spectra during fluorescence (Figure 1e and f). When monitored at 800-nm emission, the PLE spectrum consists of three bands centered at 330, 434 and 619 nm. In view of the position differences, the bands at 619 and 434 nm correspond to the Cr³⁺ d-d transition [⁴A₂ → ⁴T₂ (t²e)] and [⁴A₂ → ⁴T₁ (t²e)].^{2,9,15} It is important to note that the origin of the excitation band at ~280–320 nm in PLE spectra of Cr³⁺-doped persistent phosphors is still under debate.^{1,2,9,13,15,30} Pan *et al.* noted that the 320 nm band in bulk Zn₃Ga₂Ge₂O₁₀:Cr³⁺ originates from the ⁴A₂–⁴T₁ (te²) transition of Cr³⁺ but that the 300 nm band of LiGa₅O₈ also should be assigned to the ⁴A₂–⁴T₁ (te²) transition.^{1,13} Bessiere *et al.* concluded that the excitation band at 260–290 nm in ZnGa₂O₄: Cr³⁺ can be attributed to the overlap of the [⁴A₂–⁴T₁ (te²)] transition and the charge transfer band because it was difficult to distinguish between the Cr³⁺ [⁴A₂–⁴T₁ (te²)] band and the 4.5 eV charge transfer band.^{2,9} However, Tanabe from the Kyoto University showed clearly that the inter-transition from the Cr³⁺ ground state to the conduction band [⁴A₂–CB] at ~330 nm in the ZnGa₂O₄: Cr³⁺ phosphor overlaps the [⁴A₂–⁴T₁ (te²)] transition. Therefore, the band at 330 nm should be assigned to the overlap of the [⁴A₂ → ⁴T₁ (te²)] and [VB → CB] transitions.^{2,9,15} Considering that the optical band gap of Zn₂SnO₄ is ~3.8 eV, it is difficult to distinguish between the Cr³⁺ [⁴A₂ → ⁴T₁ (te²)] band and the 3.8 eV charge transfer band because they overlap each other.^{2,9,15} Upon excitation at 330 nm, sample ZS3 exhibits a broad emission band peaking at 800 and a sharp emission at 703 nm.

Theoretical models and experimental evidence have motivated the choice of gallates, such as LiGa₅O₈, ZnGa₂O₄ and Zn₃Ga₅Ge₂O₁₀, as admittedly excellent hosts of NIR LPPs because of the strong crystal field around Cr³⁺ ions and the ability of Cr³⁺ ions to substitute for Ga³⁺ ions. A strong crystal field is beneficial for achieving narrow-band emissions (usually near 700 nm) resulting from the spin-forbidden [²E → ⁴A₂] transition and a broadband emission (at 650–1000 nm) deriving from the spin-allowed [⁴T₂ (t²e) → ⁴A₂] transition. However, it is notable that Cr³⁺ replaces Ga³⁺ in octahedral coordination and that the crystal field strength experienced by the ion (that is, a strong, intermediate or weak crystal field) depends strongly on the crystal field environment of the host lattice.³⁰ Humeyra *et al.* have developed a method of site-selective spectroscopy to detect the presence of multiple sites available to optically active ions (Cr³⁺) in host lattices.³¹ Two types of emission bands are observed in Y₃Al₅O₁₂ (YAG), Gd₃Ga₅O₁₂ (GGG), Gd₃Sc₂Ga₃O₁₂ (GSGG) and Ca₂Y₂Mg₂Ge₃O₁₂ (CYMGG) phosphors. As the crystal field strength weakens (that is, YAG → GGG → GSGG → CYMGG), the sharp lines become more prominent in comparison with the broad band. A similar broad emission band caused by the weak crystal field is also observed in Cr³⁺-doped-K₂LiScF₆, Al(PO₃)₃, LiNbO₃ crystals and sillimanite.³² Therefore, the broad emission band in Cr-doped Zn₂SnO₄ phosphor should be assigned to the transition of Cr³⁺ [⁴T₂ (t²e) → ⁴A₂] and the sharp emission should be assigned to the vibrational sidebands of the zero-phonon R-line with phonon assistance.

As mentioned above, Zn₂SnO₄ has a typical inverse spinel crystal structure. Considering that the Zn²⁺ ions in tetrahedral sites are not

replaced because of the huge octahedral stabilization energy for Cr³⁺, chromium is assumed to precipitate at the octahedral site of Sn⁴⁺ or Zn²⁺ under a weak crystal field. Considering the similar ionic radius of Cr³⁺ (0.0615 nm), Sn⁴⁺ (0.069 nm) and Zn²⁺ (0.074 nm), it is difficult to identify which coordination polyhedron surrounds the Cr³⁺ ion. However, the effectiveness of Cr³⁺ substitution for the non-Ga³⁺ sites (Zn²⁺ or Sn⁴⁺ sites) in the octahedral lattice sites of an inverse spinel crystal seems clear. To verify this hypothesis, Cr-doped Zn₂GeO₄ and Zn₂SiO₄ phosphors were prepared. These samples exhibited no NIR persistent phosphorescence (Figure 1c). Zn₂GeO₄, which has a phenakite structure that is isostructural with the willemite Zn₂SiO₄, is different from the inverse and normal spinel structures.³³ Zn²⁺, Ge⁴⁺ and Si⁴⁺ ions occupy the site with tetrahedrally symmetric ZnO₄, GeO₄ and SiO₄ tetrahedral units in Zn₂GeO₄ and Zn₂SiO₄, which may suppress the easy intrusion of impurity ions (Supplementary Figure S1 b, c).

Tailoring controllable wavelength emission and persistence time

The process of persistent phosphorescence occurs through a delicate interplay between the energy levels of dopants or intrinsic defects and energy bands of the host lattice. Small changes in the material composition, purity type and dopant concentration can lead to variation in spatial distance between the substitutional or intrinsic defects and the conduction band. They also strongly influence the phosphorescence properties. Furthermore, the emission wavelength of TM ions strongly depends on the crystal field environment surrounding the activation ions; thus, composition variation can shift the emission band. As expected, emission wavelength tuning and persistence time tuning can be achieved by introducing a single dopant.

We demonstrate that Zn_{2-x}Al_{2x}Sn_{1-x}O₄ phosphors, which are achieved by doping Al into the Zn₂SnO₄ phosphor, allow for the extensive control of photoemission wavelength and persistence time, as shown in Figure 2. The obvious blue-shift of dominant emission peaks from 800 to 720 nm of Zn_{2-x}Al_{2x}Sn_{1-x}O₄ (from samples ZS3 to ZS10, x = 0, 0.001, 0.005, 0.01, 0.05, 0.1, 0.2 and 0.4) phosphors are demonstrated; these resemble the afterglow emission spectra shown in Figure 2c, indicating effective control and manipulation of the local crystal field around Cr³⁺ sites. The legible main luminescence peaks observed in all samples are divided into three parts ([I], [II] and [III] with the peak positions at 702, 725 and 735–800 nm, respectively). With increasing Al content, the positions of the sharp emission peaks ([I] and [II]) centered at 702 and 725 nm and associated with vibronic side bands remain constant (Figure 2b), whereas the position of the broad band [III] shifts to the high-energy side (735 nm) from the low-energy side (800 nm). However, it is notable that the ratio of integrated intensity of the sharp emission versus the broad band (I_[III]/I_[I]) varies from one phosphor to another. For the 0.1%-doped sample ZS4, the broad band is 2.5 times more intense than the emission from the 2E level; when the concentration of Al ions increases, however, the ratio decreases. For the 40% sample ZS10, the broad band is 1.2 times weaker than the vibronic side bands. The afterglow emission spectra also exhibit similar variation, as inferred from the investigation of peak position and intensity (Supplementary Figure S4). According to crystal field theory, splitting is induced by the distortion of ligands. Therefore, it is reasonable to suppose that blue-shifting of the emission band arises from the variation in crystal field parameters. This variation requires further investigation.

Both the tunable emission wavelength and the relatively complex scheme for tuning persistence time are illustrated in Figure 2d, which shows an initial decrease (from samples ZS3 to ZS6), subsequent increase (from samples ZS6 to ZS9) and final decrease again

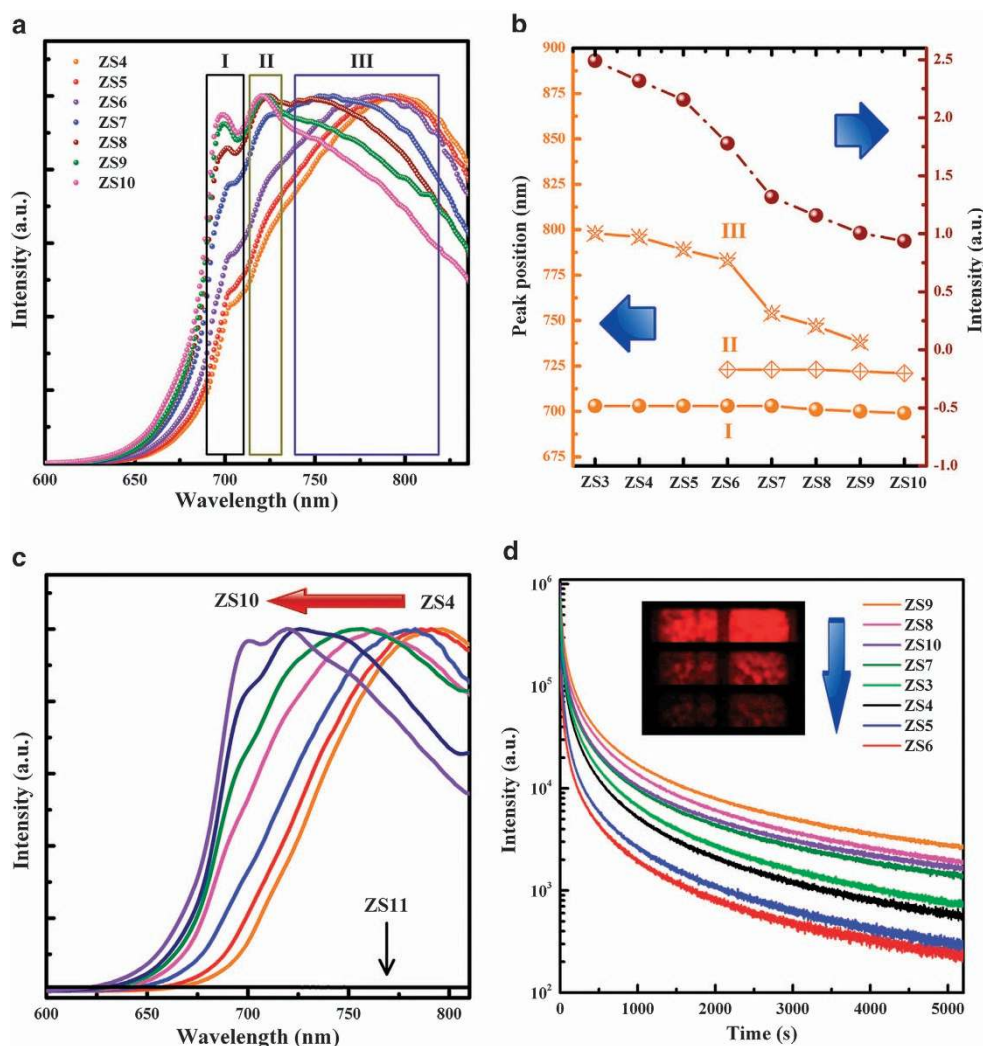


Figure 2 Tunable emission wavelength and persistence time. (a) Normalized PL spectra as a function of Al concentration excited at 320 nm (that is, $Zn_{2-x}Al_{2x}Sn_{1-x}O_4$, $x=0.001, 0.005, 0.01, 0.05, 0.1, 0.2$ or 0.4); (b) dependence of emission peak positions ([I] [II] and [III] labeled in Figure 2a (orange dots) and intensity ratio of the emission peaks [III]/[I] (brown dots) as a function of Al concentration; (c) normalized long-persistence phosphorescence spectra as a function of Al concentration. The measurements were taken at 1 min after irradiation ceased; (d) persistence time monitored at respective optimized emission wavelengths of the samples ZS3–ZS10 (that is, 800, 798, 792, 783, 753, 741, 722 and 722 nm). The inset shows near-infrared images of samples ZS3 (1 g, left) and ZS9 (1 g, right) acquired at different time intervals (15 min, 12 and 24 h); camera parameters were unchanged during the imaging process.

(from ZS9 to ZS10 samples), which may result from the variation of trap distribution due to changes in the components. We also demonstrate that NIR persistent phosphorescence can be clearly imaged, even 24 h after irradiation (inset of Figure 2d). The absolute and relative afterglow intensities of sample ZS9 as a function of time are also shown and are used to assess the practical usefulness of these novel phosphors (Supplementary Figure S5). We conclude that the phosphors presented here are nearly ideal candidates for implementation into a robust bio-probe with long-term detection capability (that is, far > 40 h). The estimated absolute afterglow intensity at 10 min and 1 h after ceasing excitation of sample ZS9 are 700 and 50 $nW\text{ cm}^{-2}$, which are slightly inferior to those of the best NIR phosphor identified to this point, $Zn_3Ga_2Ge_2O_{10}$ (1230 and 140 $nW\text{ cm}^{-2}$).¹ Here it was observed that sample ZS11 ($Zn_{1.2}Al_{1.6}Sn_{0.2}O_4$) does not show any NIR persistent phosphorescence because of the transformation of the crystalline structure (Supplementary Figure S2). It is commonly hypothesized that

phosphorescence is correlated with trapping and thermal de-trapping of charge carriers at intrinsic or extrinsic defect centers.³⁴ Considering a high-temperature sintering environment, the formation of some vacancies, such as Zn^{2+} vacancies (V_{Zn}), Sn^{4+} vacancies (V_{Sn}) or O^{2-} vacancies (V_O), may be promoted as a result of lattice disorder. The dissolution of Al^{3+} may facilitate the decrease in concentrations of some defects because Al^{3+} is assumed to precipitate at the octahedral sites of Zn^{2+} and Sn^{4+} . The introduction of Al^{3+} may also promote the generation of new imperfections when the dopant dose exceeds a certain level.

Manipulation of trap distribution

To conduct a prospective study to explore the nature of traps and hence to evaluate the trap properties, diverse and systematic investigation was performed. There is no standard way to describe the trap distribution for a given persistent phosphor. Three main features are generally considered: trap depth, concentration and type. ESR is

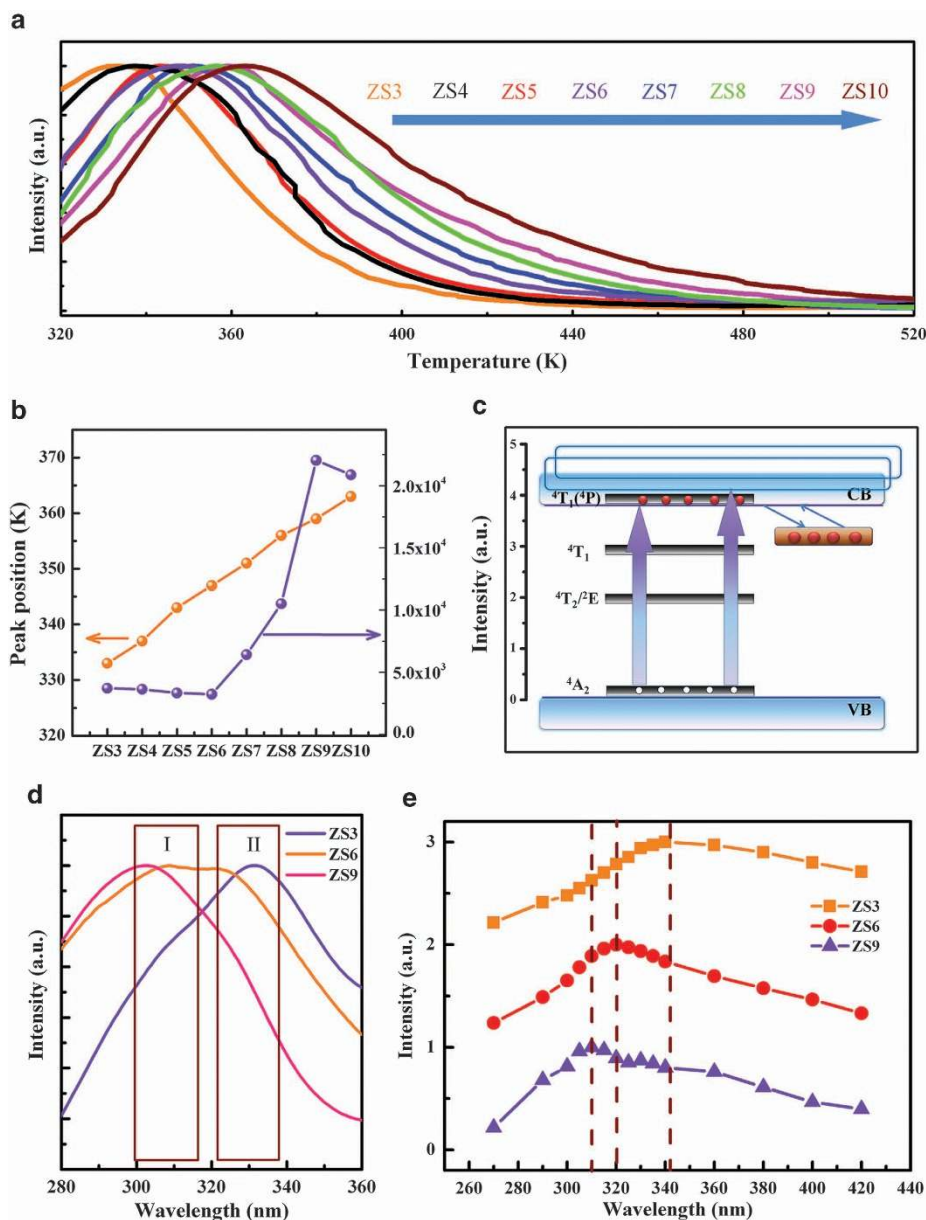


Figure 3 Tunable trap depths and concentrations. (a) Normalized thermoluminescence (TL) curves of samples ZS3–ZS10 measured 30 s after irradiation ceased; (b) TL peak positions and intensities as a function of Al doping content. (c) Schematic energy level diagram of Cr³⁺-doped Zn_{2-x}Al_{2x}Sn_{1-x}O₄ phosphors. The bottom of the conduction band (CB) is shifted upward by Al doping. (d) Normalized ultraviolet excitation spectra of samples ZS3, ZS6 and ZS9 monitored at 800, 783 and 722 nm. (e) Normalized afterglow excitation spectra monitored at 800, 783 and 722 nm of the samples ZS3, ZS6 and ZS9, respectively. (that is, afterglow intensity I_{20s} as a function of the excitation wavelengths over the 270–420 nm spectral range;¹ I_{20s} means the afterglow intensity recorded 20 s after irradiation ended).

usually used to determine trap type. Trap depth and concentration, which are additional important factors that affect persistence time, are analyzed using TL curves.^{34–36}

Trap depth manipulation via band gap variation. Shallow traps are easily emptied, whereas deep traps are difficult to empty at room temperature; a portion of captured electrons remain stored there.³⁷ TL experiments are useful for evaluating trap depths. The shift of a TL peak to a higher temperature usually indicates that the ratio of deep traps to total traps has increased. Figure 3a shows normalized TL curves for samples ZS3–ZS10 measured 30 s after irradiation ceased; these indicate that the electron reservoirs were effectively introduced

into all of the materials. It is clear that with increasing Al³⁺ concentration, the TL peaks shift to a higher temperature (from 333 to 363 K); that is, the proportion of deep traps grows, indicating that Al dissolution is beneficial in adjusting trap depth (Figure 3b).

Engineering a suitable trap depth is essential for achieving room-temperature persistent phosphorescence. If a trap is too deep, the captured electrons cannot escape, preventing persistent phosphorescence, as shown with sample ZS11 (Supplementary Figure S6). Tanabe and colleagues¹⁵ have proposed that the TL peaks of Zn(Ga_{1-x}Al_x)₂O₄:Cr,Bi phosphors monotonically shifting toward higher temperatures may be caused by the variation in the energy level location of the CB because of the substitution of Al for Ga in the ZnGa₂O₄:Cr,Bi

phosphor. Here we tend to attribute the same phenomenon to the upward shifting of the CB bottom (Figure 3c), based on consideration of the ultraviolet PLE spectra (Figure 3d), afterglow excitation spectra (Figure 3e) and diffuse reflection spectra (Supplementary Figure S7). The obvious blue-shift of PLE peaks from 330 to 300 nm in Figure 3d is a consequence of the increasing Al content. It is interesting that similar variation of the excitation band (from 340 to 310 nm) is also observed in the afterglow excitation spectrum (Figure 3e). By measuring the TLE spectrum, we further confirm a distinct afterglow excitation band at 320 nm (Supplementary Figure S8).^{9,38} With the help of the diffuse reflection spectra, we determine the optical band gap of non-doped Zn₂SnO₄ and Zn_{1.8}Sn_{0.8}Al_{0.4}O₄ phosphors to be 3.79 eV and 4.21 eV, respectively, in agreement with the reported band gap of Zn₂SnO₄ (Supplementary Figure S7). Tanabe and colleagues¹⁵ also have noted that the CB is more effective for electron trapping

[⁴A₂-CB-trap] in comparison with the [⁴A₂-⁴T₁ (te²)-CB-trap] process. By synthetically considering the variation in band gap, PL, afterglow and TLE spectra, the PLE band at 330 nm in Cr³⁺-doped Zn₂SnO₄ phosphor and 300 nm in Cr³⁺-doped Zn_{1.8}Sn_{0.8}Al_{0.4}O₄ phosphor should be assigned to the overlap of transition ⁴A₂ → ⁴T₁ (⁴P) and VB → CB, whereas the afterglow excitation band at 340 and 310 nm should be attributed to the ⁴A₂ → CB transition.

The dominated band shifting to higher energies with increasing Al doping content indicates that trap depths could be easily monitored by checking the energy level location of the conduction band. In that case, the continual shift upward of the CB would be associated with trap deepening. However, it is difficult to estimate the independent effect of an increasing energy gap between the CB level and the trap site level, especially considering the disordered variation in persistence time. Therefore, additional investigation is recommended.

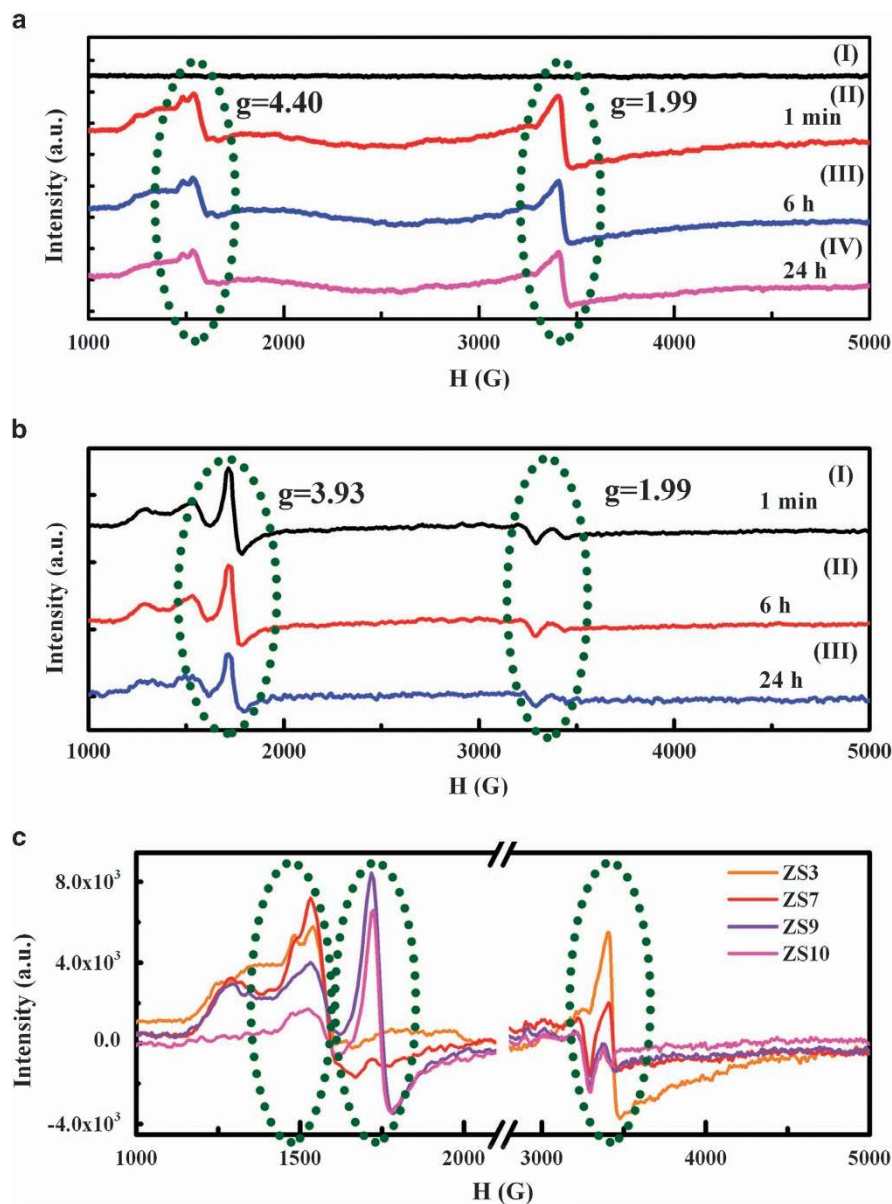


Figure 4 Tunable trap types. (a) Electron spin resonance (ESR) spectra of sample ZS3 measured before irradiation (I) and at 1 min (II), 6 h (III) and 24 h (IV) after irradiation ended, respectively. (b) ESR spectra of sample ZS9 measured at 1 min (I), 6 h (II) and 24 h (III), after irradiation ended, respectively. (c) ESR spectra of samples ZS3, ZS7, ZS9 and ZS10 measured at 1 min after irradiation ended.

Manipulation of trap concentrations and types via defect dynamic variation. Trap concentration strongly influences persistence time; or rather the quantity of electrons released from the reservoirs is directly proportional to the persistence time. To further explore the origin of the variation, it is necessary to investigate the trap concentration. In previous work, the study in trap depth and concentration in the trapping system has been conducted by performing TL experiments with different excitation wavelengths, after being excited at different temperatures, by partial thermal emptying of the traps before the experiments or at different intervals. The TL curves obtained under different conditions represent a powerful tool to uncover valuable information concerning the traps and their role in determining the spectroscopic properties of materials. Indeed, partial thermal cleaning, excitation by the light with different wavelengths and evaluation over a longer test interval, all lead to deeper traps being filled and shallower traps being emptied. Alternatively, the concentration variation of the captured and released electrons is triggered at different measurement time intervals.³⁹

TL intensities as a function of Al doping content measured 30 s after the end of irradiation are shown in Figure 3b. In contrast to the TL peak position, we confirm the typical TL intensity pattern of an initial decrease (samples ZS3–ZS6) followed by an increase (samples ZS6–ZS9) and final decrease again (samples ZS9–ZS10), which is consistent with the variation in the persistence time. Supplementary Figure S9 shows TL curves recorded 24 h after ceasing irradiation. It can be observed that the variation in Supplementary Figure S9 bears a striking similarity to the variation in Figure 3b, leaving only a tiny difference in sample ZS10 (the trap concentration of sample ZS10 is larger than that of sample ZS9, contrary to the results from Figure 3b), which further confirms that (1) the final decrease in persistence time between ZS9 and ZS10 samples is attributed to the deepening of trap depth owing to the upward shift of CB with excess incorporation of Al; (2) TL peak intensity is in direct proportion to trap concentration for samples ZS3–ZS9 excluding the minor factor of trap depths. Therefore, an initial decrease of persistence time may result from the

reduction in trap concentrations, involving the interfusion of Al³⁺ that causes the annihilation of effective defects. However, the trend of increasing persistence time may arise because the superfluous Al begins to produce new defects, which would tend to increase the persistence time. In this case, further investigation of trap types may be the key to unlock the puzzle.³⁴

Figure 4a and b shows ESR spectra of samples ZS3 and ZS9 before irradiation and at different time intervals (1 min, 6 and 24 h) after irradiation ended at 100 K. Signals with $g=4.40$ (Trap [I]) and $g=1.99$ (Trap [II]) were both detectable after irradiation, in contrast to a lack of signal before irradiation (Figure 4a). Meanwhile, signals with $g=4.40$, $g=3.93$ (Trap [III]) and $g=1.99$ could also be detected in sample ZS9 after irradiation (Figure 4b). ESR signals were all observed to decrease as the test intervals increased, indicating that (i) the detected ions or defects are responsible for electron storage; (ii) with increasing Al content, trap types vary dynamically as a result of different structural environment settings.³⁹ In addition, ESR spectra of ZS3, ZS7, ZS9 and ZS10 samples measured 1 min after irradiation ended at 100 K are also shown in Figure 4c. It is observed that the ESR spectrum exhibits an intense resonance signal with $g=1.99$ (Trap [II]) and $g=4.40$ (Trap [I]) in the ZS3 and ZS7 samples and a weak signal with $g=3.93$ (Trap [III]) in the ZS7 sample, but it also exhibits intense resonance signals with g value at $g=3.93$ along with some weak resonance signals with g value at $g=1.99$ and $g=4.40$ in the ZS9 and ZS10 samples. It is shown that the trap types of samples ZS7–ZS10 and ZS3–ZS6 remain unchanged, in agreement with the TL spectra. Therefore, we believe that the initial decrease in persistence time with increasing Al doping dose from 0 to 1% (sample ZS3–ZS6) causes the reduction of trap [II] concentration. When the Al doping dose reaches 5% (sample ZS7), the phosphors exhibit an extended persistence time owing to the rise of trap [I] concentration and the generation of a new trap [III]. Therefore, the subsequent increase from sample ZS7 to ZS9 of afterglow duration can be attributed to the increase in trap [III] concentration. Further confirmation is supplied in Supplementary Figure S10. The quantitative relationship between phosphorescence decay dynamics and ESR results illustrates the linear relationship between the afterglow intensity and the ESR signal intensity as a function of time.

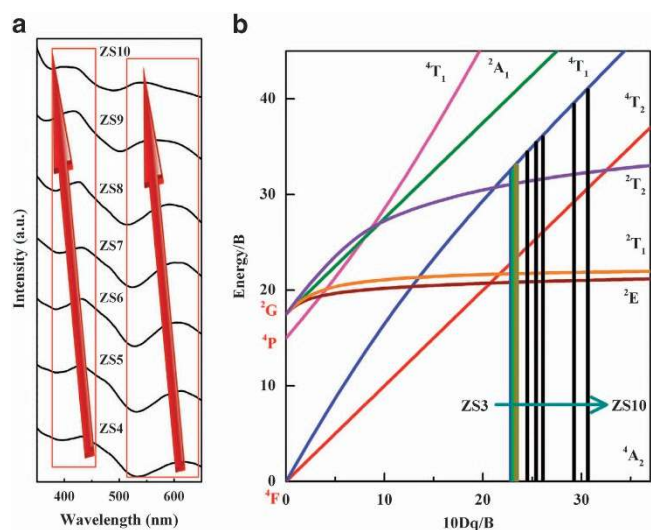


Figure 5 Tunable crystal fields. (a) Normalized visible excitation spectra of Cr³⁺-doped Zn_{2-x}Al_{2x}Sn_{1-x}O₄ ($x=0.001, 0.005, 0.01, 0.05, 0.1, 0.2$ or 0.4) phosphors. The samples were pre-annealed at 600 K. (b) Tanabe-Sugano diagram in which the straight lines indicate the normalized crystal fields of Cr³⁺ in Zn_{2-x}Al_{2x}Sn_{1-x}O₄ phosphors.

Manipulation via ligand field strength

So far, we have confirmed that Cr³⁺ only appears at the octahedral sites of Sn⁴⁺ or Zn²⁺ with a weak crystal field in Zn₂SnO₄. We also have observed the emission wavelength variation of Cr³⁺ in Zn_{2-x}Al_{2x}Sn_{1-x}O₄ phosphors. Here we believe that the emission bands strongly depend on the crystal field environment around Cr³⁺, as well as crystal field strength is influenced by composition variation. The absorption/excitation/diffuse reflection spectra related to efficient electronic transitions can be used to extract detailed information about the energy level distributions.

The importance of controlling crystal field parameter when tailoring the luminescent properties of Cr³⁺ is demonstrated in Figure 5. The crystal field parameters of Cr³⁺ ions in Zn_{2-x}Al_{2x}Sn_{1-x}O₄ phosphors are calculated and presented in Table 2 and demonstrating an increase in crystal field strength, with the help of the Tanabe–Sugano matrix.⁴⁰ The relatively precise crystal field strength Dq and the Racah parameters B can be estimated by spectroscopic data as follows:¹⁷

$$10Dq = \nu_2 \quad (1)$$

$$B = (\nu_1^2 + 2\nu_2^2 - 3\nu_1\nu_2)/(15\nu_1 - 27\nu_2) \quad (2)$$

where ν_1 and ν_2 are the energy corresponding to [$^4A_2 \rightarrow ^4T_1$ (t^2e)] and [$^4A_2 \rightarrow ^4T_2$ (t^2e)] transitions of Cr³⁺ ions, respectively.

Struve *et al.*²⁶ have investigated the basic spectroscopic properties of Cr³⁺-doped gallium garnets. Weak crystal fields ($Dq/B=2.39\text{--}2.55$) lead to broad $^4T_2\text{--}^4A_2$ fluorescence in the 700–950 nm range depending on the chemical composition of the crystals. In their research, to obtain relatively weak crystal fields, the Cr³⁺–O²⁻ distances had to be increased compared to YAG (Y₃Al₅O₁₂). This was achieved by the incorporation of Ga³⁺, Sc³⁺, Lu³⁺, Gd³⁺ or La³⁺ with their larger ionic radii compared with Al³⁺ or Y³⁺, respectively. The weaker crystal fields of samples ZS3–ZS8 ($Dq/B=2.292\text{--}2.609$) in the current work are shown to confirm the broad emission band resulting from the $^4T_2\text{--}^4A_2$ transition. With increasing Al doping, two excitation peaks of Cr³⁺ display an adjustable blue shift. It is most likely the case that Al³⁺ ions are incorporated into the crystal phase by replacing octahedral Zn²⁺ and Sn⁴⁺ in the disordered ZnO₆ and SnO₆ octahedron, which is consistent with the XRD results (Supplementary Figure S2). By shortening the Cr³⁺–O²⁻ distances, achieved by the incorporation of Al³⁺ (53 pm) with its smaller ionic radii compared with Zn²⁺ (74 pm) and Sn⁴⁺ (69 pm), the crystal field strength of Cr³⁺ increases. As a result, there is an increase in energy level splitting, resulting in a shift in excitation and emission wavelengths.^{26,41} Furthermore, the ZnAl₂O₄ secondary phase, with its stronger crystal field, appears in the Zn_{2-x}Al_{2x}Sn_{1-x}O₄ system because of the higher Al content. The increase in crystal field strength causes blue shifting in the dominant excitation and emission peaks associated with the Cr³⁺ centers in the Zn_{2-x}Al_{2x}Sn_{1-x}O₄ phosphors, indicating that the peak locations can be precisely tuned.

Table 2 Estimated crystal field parameters of Cr³⁺ in the samples ZS3–ZS10 (Zn_{2-x}Al_{2x}Sn_{1-x}O₄: 0.2% Cr³⁺, $x=0, 0.001, 0.005, 0.01, 0.05, 0.1, 0.2, 0.4$)

	$^4A_2 \rightarrow ^4T_1$ [nm]	$^4A_2 \rightarrow ^4T_2$ [nm]	Dq [cm ⁻¹]	B [cm ⁻¹]	Dq/B
ZS3	434	619	1616	705	2.292
ZS4	432	615	1626	703	2.312
ZS5	431	612	1634	698	2.340
ZS6	431	606	1650	673	2.450
ZS7	430	600	1667	656	2.539
ZS8	426	591	1692	649	2.609
ZS9	418	566	1767	604	2.925
ZS10	402	539	1855	605	3.066

It should be noted that, to the best of our knowledge, this type of NIR long-persistence phosphorescence has not been previously reported to occur in non-gallate materials.^{1,2,17,18,21} Hereby, both wavelength tuning and trap distribution tuning are successfully demonstrated by our one-step modification strategy. Further details that clarify the process of tailoring structure variation are given in the supporting information, which includes data from XRD and XPS measurements (Supplementary Figure S11). The results conclusively demonstrate the convenience and effectiveness of fabricating this type of LPP by intelligently tailoring the crystal field around the active center and by deploying the trap distributions.⁴²

Schematic energy level diagrams

Figure 6 shows schematic energy level diagrams for the electron trapping–detrapping process in Cr³⁺-doped Zn_{2-x}Al_{2x}Sn_{1-x}O₄ phosphors. (i) The Cr³⁺ ion can substitute for Zn²⁺ or Sn⁴⁺ in the distorted octahedral coordination because of their identical ionic radii and the tendency for defect formation that arises in the characteristic inverse spinel crystal structure in the form of non-equivalent substitution. Thus, the present work demonstrates the synthesis of low-cost Zn₂SnO₄: Cr phosphors with a characteristic inverse spinel structure and occupation of the non-Ga³⁺ site by Cr³⁺. A variety of imperfections, such as antisite defects, Zn vacancies, oxygen vacancies and others have been proposed as electron reservoirs (Figure 6a). (ii) Tuning of both emission band and persistence time is successfully demonstrated through Al doping. With increasing Al content, the dominant excitation and emission peaks of Cr³⁺ centers in Zn_{2-x}Al_{2x}Sn_{1-x}O₄ phosphors all exhibit blue shifting caused by the increasing crystal field strength. (iii) Simultaneously, this process is coupled with an upward shift of the conduction band, causing trap depths to deepen (Figure 6b). This method also relies on the variation in the trap concentration and type with Al content. When the dopant dose is small, trap types remain consistent but the concentrations decrease because the interdiffusion of small concentrations of Al³⁺ involves the annihilation of effective defects. However, when considering a larger dopant dose, the spontaneous creation of new defects increases the persistence time (Figure 6c), which constitutes our strategy for controlling persistence time.⁴³

In summary, we report the fabrication of earth-abundant and inexpensive NIR phosphorescent Cr³⁺-doped non-gallate materials (Zn₂SnO₄: Cr and Zn_(2-x)Al_{2x}Sn_(1-x)O₄: Cr). The Zn₂SnO₄: Cr phosphor features an emission band from 650 to 1200 nm, peaking at 800 nm. We also demonstrate the high effectiveness of inserting Cr³⁺ into non-Ga³⁺ locations in the octahedral lattice sites of an

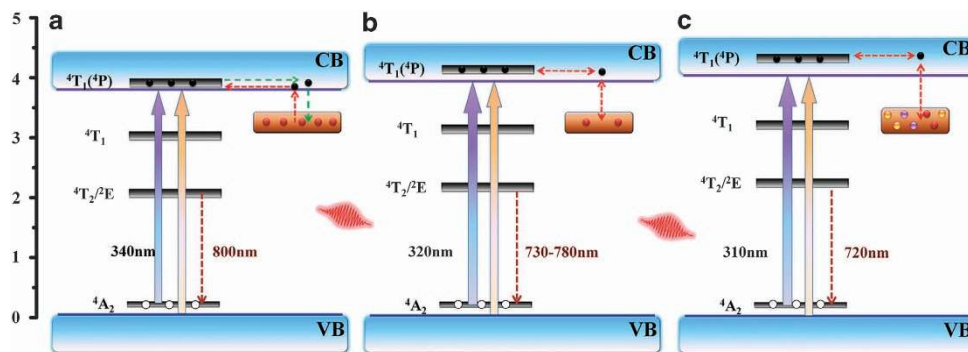


Figure 6 Schematic energy level diagrams for the electrons trapping–detrapping process in Cr³⁺-doped Zn_{2-x}Al_{2x}Sn_{1-x}O₄ phosphors, $x=0$ (a), 0.01 (b) and 0.2 (c), respectively. The red sphere represents the original trap site; the additional yellow and purple spheres represent the newly created trap site.

inverse spinel crystal by comparing the optical properties of Zn₂SnO₄, Zn₂GeO₄ and Zn₂SiO₄ phosphors. In addition, this research demonstrates the validity of precisely tailoring the local crystal field around the active center and of controlling trap distribution by changing the composition of Zn_(2-x)Al_{2x}Sn_(1-x)O₄ solid solutions to obtain the desired photoemission wavelength and persistence time. The infrared phosphorescence peak positions can be precisely tuned from 800 to 720 nm by adding Al, with resulting rearrangement of the ligands surrounding Cr³⁺. With an increasing Al content, a deepening of trap levels is observed through TL measurements; this deepening arises from the increase in energy gap between the CB level and the trap site level. We demonstrate that the variation in trap concentration and type, which is determined by the dynamic variation of defect annihilation and creation, is closely correlated with the phosphorescence duration as measured in ESR and TL experiments. Further research is underway on the nanocrystallization and functionalization of LPPs, which are expected to open up new possibilities for visualizing structural and functional processes in cells, tissues and other complex systems.⁴⁴

CONFLICT OF INTEREST

The authors declare no conflict of interest.

ACKNOWLEDGEMENTS

This work was financially supported by the National Natural Science Foundation of China (Grant nos. 51132004, 51322208, 51102096 and 51302087), and by the Guangdong Natural Science Foundation (Grant nos. 2014A030310444, S20120011380 and S2013050014549).

- Pan, Z., Lu, Y. Y. & Liu, F. Sunlight-activated long-persistent luminescence in the near-infrared from Cr³⁺-doped zinc gallogermanates. *Nat. Mater.* **11**, 58–63 (2012).
- Maldiney, T., Bessiere, A., Seguin, J., Teston, E., Sharma, S. K., Viana, B., Bos, A. J. J., Dorenbos, P., Bessodes, M., Gourier, D., Sherman, D. & Richard, C. The *in vivo* activation of persistent nanophosphors for optical imaging of vascularization, tumours and grafted cells. *Nat. Mater.* **13**, 418–426 (2014).
- Boyer, C., Whittaker, M. R., Bulmus, V., Liu, J. Q. & Davis, T. P. The design and utility of polymer-stabilized iron-oxide nanoparticles for nanomedicine applications. *NPG Asia Mater.* **2**, 23–30 (2010).
- Liu, Y. S., Tu, D. T., Zhu, H. M. & Chen, X. Y. Lanthanide-doped luminescent nanoprobes: controlled synthesis, optical spectroscopy, and bioapplications. *Chem. Soc. Rev.* **42**, 6924–6958 (2013).
- Chen, Z., Zheng, W., Huang, P., Tu, D. T., Zhou, S. Y., Huang, M. D. & Chen, X. Y. Lanthanide-doped luminescent nano-bioprobes for the detection of tumor markers. *Nanoscale* **7**, 4274–4290 (2015).
- Gu, L., Hall, D., Qin, Z., Anglin, E., Joo, J., Mooney, D. J., Howell, S. B. & Sailor, M. J. *In vivo* time-gated fluorescence imaging with biodegradable luminescent porous silicon nanoparticles. *Nat. Commun.* **4**, 2326(1)–2326(7) (2013).
- Frangioni, J. V. *In vivo* near-infrared fluorescence imaging. *Curr. Opin. Chem. Biol.* **5**, 626–634 (2003).
- Chermont, Q., Chaneac, C., Seguin, J., Pelle, F., Maitrejean, S., Jolivet, J. P., Gourier, D., Bessodes, M. & Scherman, D. Nanoprobes with near-infrared persistent luminescence for *in vivo* imaging. *Proc. Natl Acad. Sci. USA* **104**, 9266–9271 (2007).
- Bessiere, A., Sharma, S. K., Basavaraju, N., Priolkar, K. R., Binet, L., Viana, B., Bos, A. J. J., Maldiney, T., Richard, C., Scherman, D. & Gourier, D. Storage of visible light for long-lasting phosphorescence in chromium-doped zinc gallate. *Chem. Mater.* **26**, 1365–1373 (2014).
- Maldiney, T., Lecointre, A., Viana, B., Bessiere, A., Bessodes, M., Gourier, D., Richard, C. & Scherman, D. Controlling electron trap depth to enhance optical properties of persistent luminescence nanoparticles for *in vivo* imaging. *J. Am. Chem. Soc.* **133**, 11810–11815 (2011).
- Allix, M., Chenu, S., Veron, E., Poumeyrol, T., Kouadri-Boudjelthia, E. A., Alahache, S., Porcher, F., Massiot, D. & Fayon, F. Considerable improvement of long-persistent luminescence in germanium and tin substituted ZnGa₂O₄. *Chem. Mater.* **25**, 1600–1606 (2013).
- Abdukayum, A., Chen, J. T., Zhao, Q. & Yan, X. P. Functional near infrared-emitting Cr³⁺/Pr³⁺ co-doped zinc gallogermanate persistent luminescent nanoparticles with superlong afterglow for *in vivo* targeted bioimaging. *J. Am. Chem. Soc.* **135**, 14125–14133 (2013).
- Liu, F., Yan, W., Chuang, Y. J., Zhen, Z., Xie, J. & Pan, Z. Photostimulated near-infrared persistent luminescence as a new optical read-out from Cr³⁺-doped LiGa₅O₈. *Sci Rep.* **3**, 1554(1)–1554(7) (2013).
- Li, Y., Zhou, S. F., Dong, G. P., Peng, M. Y., Wondraczek, L. & Qiu, J. R. Anti-stokes fluorescent probe with incoherent excitation. *Sci Rep.* **4**, 4059(1)–4059(6) (2013).
- Zhuang, Y. X., Ueda, J. & Tanabe, S. Tunable trap depth in Zn(Ga_{1-x}Al_x)₂O₄: Cr, Bi red persistent phosphors: considerations of hightemperature persistent luminescence and photostimulated persistent luminescence. *J. Mater. Chem. C* **1**, 7849–7856 (2013).
- Li, Y., Zhou, S. F., Li, Y. Y., Sharafudeen, K., Ma, Z. J., Dong, G. P., Peng, M. Y. & Qiu, J. R. Long persistent and photo-stimulated luminescence in Cr³⁺-doped Zn–Ga–Sn–O phosphors for deep and reproducible tissue imaging. *J. Mater. Chem. C* **2**, 2657–2663 (2014).
- Chen, D. Q., Chen, Y., Lu, H. W. & Ji, Z. G. A bifunctional Cr/Yb/Tm: Ca₃Ga₂Ge₃O₁₂ phosphor with near-Infrared long-lasting phosphorescence and upconversion Luminescence. *Inorg. Chem.* **53**, 8638–8645 (2014).
- Jia, D., Lewis, L. A. & Wang, X. J. Cr³⁺-doped lanthanum gallogermanate phosphors with long persistent IR emission. *Electrochem. Solid-State Lett.* **13**, J32–J34 (2010).
- Ueda, J., Kuroishi, K. & Tanabe, S. Bright persistent ceramic phosphors of Ce³⁺-Cr³⁺ co-doped garnet able to store by blue light. *Appl. Phys. Lett.* **104**, 101904(1)–101904(4) (2014).
- Sharma, S. K., Gourier, D., Viana, B., Maldiney, T., Teston, E., Scherman, D. & Richard, C. Persistent luminescence of AB₂O₄: Cr³⁺ (A = Zn, Mg, B = Ga, Al) spinels: New biomarkers for *in vivo* imaging. *Opt. Mater.* **11**, 1901–1906 (2014).
- Smith, A. M., Mancini, M. C. & Nie, S. Bioimaging: second window for *in vivo* imaging. *Nat. Nanotechnol.* **4**, 710–711 (2009).
- Caratto, V., Locardi, F., Costa, G. A., Masina, R., Fasoli, M., Panzeri, L., Martini, M., Bottinelli, E., Gianotti, E. & Miletto, I. NIR persistent luminescence of lanthanide ion-doped rare-earth oxycarbonates: the effect of dopants. *ACS Appl Mater. Interfaces* **6**, 17346–17351 (2014).
- Van den Eckhout, K., Poelman, D. & Smet, P. F. Persistent luminescence in non-Eu²⁺ Doped compounds: A review. *Materials* **6**, 2789–2818 (2013).
- Dorenbos, P. The Eu³⁺ charge transfer energy and the relation with the band gap of compounds. *J. Lumin.* **111**, 89–104 (2005).
- Zhou, S. F., Jiang, N., Zhu, B., Yang, H. C., Ye, S., Lakshminarayana, G., Hao, J. H. & Qiu, J. R. Multifunctional bismuth-doped nanoporous silica glass: From blue-green, orange, red, and white light sources to ultra-broadband infrared amplifiers. *Adv. Funct. Mater.* **18**, 1407–1413 (2008).
- Struve, B. & Huber, G. The effect of the crystal field strength on the optical spectra of Cr³⁺ in gallium garnet laser crystals. *Appl. Phys. B* **36**, 195–201 (1985).
- Bao, L. H., Zang, J. F. & Li, X. D. Flexible Zn₂SnO₄/MnO₂ core/shell nanocable-carbon microfiber hybrid composites for high-performance supercapacitor electrodes. *Nano Lett.* **11**, 1215–1220 (2011).
- Zhang, S. B. & Wei, S. H. Self-doping of cadmium stannate in the inverse spinel structure. *Appl. Phys. Lett.* **80**, 1376–1378 (2002).
- Gracia, L., Beltran, A. & Andres A theoretical study on the pressure-induced phase transitions in the inverse spinel structure Zn₂SnO₄. *J. Phys. Chem. C* **115**, 7740–7746 (2011).
- Deren, P. J., Gabor, A. W. & Pazik, R. Weak crystal field in yttrium gallium garnet (YGG) submicrocrystals doped with Cr³⁺. *Cryst. Growth Des.* **12**, 4752–4757 (2012).
- Orucu, H., Ozen, G., Bartolo, B. D. & Collins, J. Site-selective spectroscopy of garnet crystals doped with chromium ions. *J. Phys. Chem. A* **116**, 8815–8826 (2012).
- Wojtowicz, A. J. & Lempicki, A. Luminescence of Cr³⁺ in sillimanite. *Phys. Rev. B* **39**, 8695–8701 (1989).
- Yan, S. Y., Wang, J. J., Gao, H. L., Wang, N. Y., Yu, H., Li, Z. S., Zhou, Y. & Zou, Z. G. Zinc gallogermanate solid solution: a novel photocatalyst for efficiently converting CO₂ into solar fuels. *Adv. Funct. Mater.* **23**, 1839–1845 (2013).
- Li, Y., Li, Y. Y., Sharafudeen, K., Dong, G. P., Zhou, S. F., Ma, Z. J., Peng, M. Y. & Qiu, J. R. A strategy for developing near infrared longpersistent phosphors: taking MAIO₃: Mn⁴⁺, Ge⁴⁺ (M = La, Gd) as an example. *J. Mater. Chem. C* **5**, 2019–2027 (2014).
- Trojan, P. J., Niittykoski, J., Holsa, J. & Zych, E. Thermoluminescence and kinetics of persistent luminescence of vacuum-sintered Tb³⁺-doped and Tb³⁺, Ca²⁺-codoped Lu₂O₃ materials. *Chem. Mater.* **20**, 2252–2261 (2008).
- Ueno, K. & Misawa, H. Plasmon-enhanced photocurrent generation and water oxidation from visible to near-infrared wavelengths. *NPG Asia Mater.* **2**, e65(1)–e65(6) (2013).
- Dorenbos, P., Van der Kolk, E., Bos, A. J. J. & Melcher, C. L. Afterglow and thermoluminescence properties of Lu₂SiO₅: Ce scintillation crystals. *J. Phys.: Condens. Matter* **6**, 4167–4181 (1994).
- Bos, A. J. J., Duijvenvoorde, R. M. V., Van der Kolk, E., Drozdowski, W. & Dorenbos, P. Thermoluminescence excitation spectroscopy: a versatile technique to study persistent luminescence phosphors. *J. Lumin.* **131**, 1465–1471 (2011).
- Li, Y., Du, X., Sharafudeen, K., Liao, C. X. & Qiu, J. R. A long persistent phosphor based on recombination centers originating from Zn imperfections. *Spectrochim. Acta A Mol. Biomol. Spectrosc.* **123**, 7–11 (2014).
- Zhou, S. F., Jiang, N., Wu, B. T., Hao, J. H. & Qiu, J. R. Ligand-driven wavelength-tunable and ultra-broadband infrared luminescence in single-ion-doped transparent hybrid materials. *Adv. Funct. Mater.* **19**, 2081–2088 (2009).

- 41 De Groot, F. M. F., Fuggle, J. C., Thole, B. T. & Sawatzky, G. A. 2p x-ray absorption of 3d transition-metal compounds: An atomic multiplet description including the crystal field. *Phys. Rev. B* **42**, 5459–5468 (1990).
- 42 Wang, J. J., Hu, J. S., Guo, Y. & Wan, L. J. Wurtzite Cu₂ZnSnSe₄ nanocrystals for high-performance organic–inorganic hybrid photodetectors. *NPG Asia Mater.* **4**, 1–6 (2012).
- 43 Aitasalo, T., Holsa, H., Jungner, H., Lastusaari, M. & Niittykoski, J. Thermoluminescence study of persistent luminescence materials: Eu²⁺ and R³⁺-doped calcium aluminates, CaAl₂O₄: Eu²⁺, R³⁺. *J. Phys. Chem. B* **110**, 4589–4598 (2006).
- 44 Van den Eeckhout, K., Smet, P. F. & Poelman, D. Persistent luminescence in Eu²⁺-doped compounds: A review. *Materials* **3**, 2536–2566 (2010).



This work is licensed under a Creative Commons Attribution 4.0 International License. The images or other third party material in this article are included in the article's Creative Commons license, unless indicated otherwise in the credit line; if the material is not included under the Creative Commons license, users will need to obtain permission from the license holder to reproduce the material. To view a copy of this license, visit <http://creativecommons.org/licenses/by/4.0/>

Supplementary Information accompanies the paper on the NPG Asia Materials website (<http://www.nature.com/am>)